1   *Article*

2   # Facile Fabrication of Multifunctional ZnO Urchins

3   **Abinash Tripathy‡¥, Patryk Wąsik‡ψ, Syama Sreedharan‖, Dipankar Nandi‖, Oier Bikondoa†,£,**

4   **Bo Su§, Prosenjit Sen¥ and Wuge H. Briscoe‡***

5   ‡ - School of Chemistry, University of Bristol, Cantock's Close, Bristol BS8 1TS, United Kingdom.

6   ¥ - Centre for Nano Science and Engineering, Indian Institute of Science, Bangalore, India, 560012.

7   ψ - Bristol Centre for Functional Nanomaterials (BCFN), HH Wills Physics Laboratory, University of Bristol,

8   Tyndall Avenue, Bristol BS8 1TL, United Kingdom.

9   ‖ - Department of Biochemistry, Indian Institute of Science, Bangalore, India, 560012.

10   † - XMas, The UK CRG Beamline at the ESRF, The European Synchrotron, 71, avenue des Martyrs, CS 40220,

11   38043 Grenoble Cedex 9, France.

12   £ - Department of Physics, University of Warwick, Gibbet Hill Road, CV4 7AL, Coventry, United Kingdom.

13   § - Bristol Dental School, University of Bristol, Bristol BS1 2LY, United Kingdom.

14   *Corresponding Author: Wuge.Briscoe@bristol.ac.uk

17   **Abstract:** Functional ZnO nanostructured surfaces are important in a wide range of applications.

18   Here we report facile fabrication of ZnO surface structures at near room temperature with

19   morphology resembling that of sea urchins, with densely packed, μm-long, tapered nanoneedles

20   radiating from the urchin centre. The ZnO urchin structures were successfully formed on several

21   different substrates with high surface density and coverage, including silicon (Si), glass,

22   polydimethylsiloxane (PDMS), and copper (Cu) sheets, as well as Si seeded with ZnO nanocrystals.

23   Time-resolved SEM revealed growth kinetics of the ZnO nanostructures on Si, capturing the

24   emergence of "infant" urchins at the early growth stage and subsequent progressive increase in the

25   urchin nanoneedle length and density, whilst the spiky nanoneedle morphology was retained

26   throughout the growth. ε-Zn(OH)$_2$ orthorhombic crystals were also observed alongside the urchins.

27   The crystal structures of the nanostructures at different growth time were confirmed by synchrotron

28   X-ray diffraction measurements. On seeded Si substrates, a two-stage growth mechanism was

29   identified, with a primary growth step of vertically aligned ZnO nanoneedle arrays preceding the

30   secondary growth of the urchins atop the nanoneedle array. The antibacterial, anti-reflective, and

31   wetting functionality of the ZnO urchins – with spiky nanoneedles and at high surface density – on

32   Si substrates was demonstrated. First, bacteria colonisation was found to be suppressed on the

33   surface after 24 h incubation in Gram-negative *E. coli* culture, in contrast to control substrates (bare

34   Si and Si sputtered with 20 nm ZnO thin film). Secondly, the ZnO urchin surface, exhibiting

35   superhydrophilic property with a water contact angle $\sim$ 0°, could be rendered superhydrophobic

36   with a simple silanization step, characterised by apparent water contact angle θ of 159°±1.4° and

37   contact angle hysteresis $\Delta\theta$ <7°. The dynamic superhydrophobicity of the surface was demonstrated

38   by bouncing-off of a falling 10 μL water droplet, with a contact time of 15.3 milliseconds (ms),

39   captured using a high-speed camera. Thirdly, it was shown that the presence of dense spiky ZnO

40   nanoneedles and urchins on the seeded Si substrate exhibited a reflectance $R < 1\%$ over the

41   wavelength range λ = 200-800 nm. The ZnO urchins with unique morphology *via* a facile fabrication

route at room temperature, readily implementable on different substrates, may be further exploited for multifunctional surfaces and product formulations.

Keywords: ZnO urchins, nanostructured surfaces, *E. coli*, superhydrophilic, superhydrophobic, anti-reflective surfaces

1. Introduction

Nanostructured surfaces are widespread in nature and many are ingeniously multifunctional. This has inspired considerable effort in fabrication of hierarchical surface nanotextures. For instance, Lotus leaf inspired nanostructures on silicon, TiO_2, polymer surfaces exhibit superhydrophobic, self-cleaning and antibacterial characteristics[1–5]. Nanostructured surfaces on silicon, glass substrates mimicking cicada/dragonfly wings or moth eye possess superhydrophobic and antimicrobial characteristics, as well as gradient refractive indices for anti-reflective applications[6–11].

Surfaces bearing ZnO nanostructures are among most widely studied, with a wide range of applications in gas and bio-sensing, field emission devices, ultra violet detectors, and photovoltaics[12], due to their thermostability[13], low-cost production[14], antimicrobial properties[15–19], and biocompatibility[20]. Several fabrication methods of ZnO nanostructured surfaces have been reported[21–28], such as hydrothermal synthesis, laser ablation, sputtering, thermal decomposition, evaporation induced self-assembly[29,30], and the sol-gel technique. Various ZnO nanostructures that have been reported include one-dimensional (1-D) morphologies such as nanowires[31–33], nanofibers[29,30], nanorods[34–37], micro-dendrites[38,39], and nanotubular structures[40–44], as well as 3-D architectures such as flowers/urchins[45–50], tetrapods/jack-like[51,52], and hedgehogs[53]. The 3-D nanostructures with enhanced surface area may be used as substitutes for 1-D nanostructure arrays with enhanced functionalities, but their fabrication requires either sophisticated instrumentation or elevated temperatures (thus high energy input).

Here, we report facile fabrication of multifunctional 3-D ZnO urchins on silicon (Si) substrates in a solution-based synthesis at near room temperature (RT) using a one-step procedure, which could also be applied on Si substrates seeded with ZnO crystals and various other substrates. The morphology of these ZnO surface structures resembles that of sea urchins, with tapered nanoneedles of   m in length radiating from a central core. The growth kinetics of the ZnO urchins was studied by examining their intermediate morphologies at different growth time intervals (0.5 - 12 h). The ZnO urchin-coated surface exhibited high anti-reflectance, and superhydrophobicity after silanization as investigated by contact angle, contact angle hysteresis and drop impact analyses. They were also bacteriophobic against *E. coli*.   The simple fabrication method for ZnO urchins could also be adapted to a variety of materials such as polydimethylsiloxane (PDMS), copper sheets and glass substrates, demonstrating its versatility.

2. Materials and Methods

2.1 Substrates preparation and cleaning

Silicon substrates were prepared by cutting a silicon wafer (100 mm diameter, P type, B dopant, <100>, 1-100 Ω·cm, 500 μm thick, single-sided polish, test grade, University Wafer, Inc.) into 1 cm x 1

83   cm squares. All substrates, including copper sheet, glass slide (Polar Industrial Corporation) and
84   polydimethylsiloxane (Dow Corning, Sylgard 184) were cleaned by a subsequent sonication in
85   acetone, ethanol, and deionized water (10 minutes in each) followed by drying with N_2.

86   *2.2 Seeding*

87   Seeding procedure was used to produce nucleation sites for the growth of ZnO nanostructures[31].
88   Cleaned silicon substrates were dipped in a solution of zinc acetate dihydrate ($Zn(CH_3COO)_2 \cdot 2H_2O$,
89   99%, Sigma Aldrich) in ethanol (CH_3CH_2OH, Absolute, Sigma Aldrich) for few seconds, rinsed with
90   clean ethanol and then dried with N_2. This coating step was repeated 5 times for each seeded silicon
91   substrate (see Figure S1). Subsequently, the substrates were heated to 300° C on a hot plate, and
92   annealed for 30 minutes in air to thermally decompose zinc acetate crystallites to ZnO islands with
93   (0001) planes parallel to the silicon substrate surface[31].

94   *2.3 ZnO Urchin growth*

95   To grow the ZnO nanostructures, 50 mL aqueous solution of zinc nitrate hexahydrate
96   ($Zn(NO_3)_2 \cdot 6H_2O$, 98%, Sigma Aldrich) solution was added dropwise to 50 mL of potassium hydroxide
97   (KOH, 85%, Fisher Scientific) aqueous solution under constant stirring for 30 minutes. Next, the alkali
98   solution of zincate ions was carefully poured to the glass Petri dish containing substrates (seeded Si,
99   non-seeded Si, Cu sheet, glass and polydimethylsiloxane, separately for each type) sealed with a glass
100   lid and a paraffin film, and kept at $20° \pm 2°C$ for 12 hours. After the synthesis, samples were rinsed
101   with DI water and dried with N_2.

102   *2.4 Bacterial growth conditions and sample preparation*

103   Isolated single colonies of *E. coli* K-12 (MG 1655) were used to prepare the pre-inoculum[54]. The
104   culture was grown in Luria Bertani (LB) medium for 8 hrs at 37°C with constant shaking at 160 rpm.
105   A 0.2 % pre-inoculum was added into 10 mL of LB medium and it was allowed to grow until 0.3
106   optical density (O. D.) at 600 nm[55]. The cells were subsequently pelleted and washed with
107   phosphate-buffered saline (PBS). A cell suspension of 0.01 O. D. at 600 nm was used for studying the
108   bacterial interaction with the bare, unmodified silicon, silicon with 20 nm thin film of ZnO and ZnO
109   nano-urchin surfaces.

110   *2.5 Scanning electron microscopy (SEM)*

111   ZnO nanostructured surfaces were imaged using field emission scanning electron microscopy (JSM-
112   IT300 SEM (JEOL)). Dimension of the ZnO nano urchin-like structures were obtained from the SEM
113   images using ImageJ software. For bacterial sample imaging, substrates were first washed with PBS
114   to remove the loosely adhered cells. Substrates were then dipped in 2.5% of Glutaraldehyde to fix the
115   cells. After that all the substrates were allowed to dry in vacuum. Thin layer of gold (15 nm) was
116   sputtered on the samples using a Quorum sputter coater (Q150T) to avoid the charging effect while
117   doing the SEM. Samples were scanned thoroughly using SEM (sample size 1.3 cm × 1.3 cm) and the
118   imaging was done in triplicates for all the samples. Selecting three specimens from each type of a
119   sample (two controls and one ZnO Urchin surface) ensured the repeatability.
120

121   *2.6 Urchin dimension analysis*

122   ImageJ[56] was used to obtain the morphological information of the nanoneedles comprising the ZnO
123   urchin and the vertical nanoneedles using the length and angle measurement tools.

124   *2.7 X-ray Diffraction (XRD)*

125   The presence of crystalline ZnO after the growth procedure was confirmed using D8 Advance
126   Bruker-AXS diffractometer (Cu Kα radiation (λ = 0.154178 nm), $\theta - 2\theta$ scan, 2θ = 10°-90°, step size
127   - 0.02 (2θ), step count - 1.5 s).

128   *2.8 Grazing incidence X-ray diffraction (GIXRD)*

129   GIXRD analysis of the seeded and non-seeded silicon substrates used to study the time dependence
130   growth of ZnO nanostructures was performed at Beamline BM28 at the European Synchrotron
131   Radiation Facility (France). Experimental parameters: radiation wavelength: 0.8856 Å, sample to
132   detector distance: 0.24 m, detector: MAR165, calibrant: Silver behenate and ZnO powder. The
133   diffraction patterns were reduced to one-dimensional line profiles using *pyFAI*, a pythonic library for
134   1D azimuthal / 2D radial integrations of diffraction images[57].

135   *2.9 Contact angle measurement and high-speed imaging*

136   Apparent contact angle[58–60] measurements were carried out using a Krüss Drop Shape Analyser
137   (DSA 100). 10 μL water droplet was placed gently on all the substrates to measure the contact angles.
138   A custom-made goniometer setup was used to measure the contact angle hysteresis. The stage of the
139   goniometer was tilted, and the droplet image was captured when the droplet first started to slide to
140   measure the contact angle hysteresis. The advancing and receding contact angle were measured from
141   the droplet image using ImageJ software. The contact angle hysteresis was obtained by calculating
142   the difference between the advancing and receding contact angles. All the measurements were
143   repeated three times. Droplet impact dynamics of water droplet on the superhydrophobic surface
144   (silanized seeded silicon substrate with ZnO nanostructures) was captured using a high-speed
145   camera (Photron FastCam SA4) at 10,000 fps (time resolution of 0.1 ms). The droplets were created
146   by a micro-pipette and released from a height of 7 cm (Weber number $(We) = \frac{inertial\ force}{surface\ tension\ force} =$

147   $\frac{\rho V^2 D_w}{\gamma} = \frac{1000 \times 1.17^2 \times 0.0026}{0.072} = 49,$

148   $Density\ of\ water\ (\rho) = 1000\frac{kg}{m^3}, Velocity\ of\ falling\ droplet\ (V) = \sqrt{2gh} =$

149   $1.17\frac{m}{s}, Surface\ tension\ of\ water\ (\gamma) = 0.072\frac{N}{m},\ and\ diameter\ of\ droplet\ (D_w) = 0.0026\ m).$

150   *2.10 Reflectance measurements*

151   To calculate the reflectance of all the surfaces, Shimadzu MPC3600 UV-VIS-NIR Spectrometer with
152   an absolute specular reflectance mode was used. Wavelengths ranging from 200 nm to 800 nm were
153   used for the reflectance measurement. D$_2$ light source was used for the range 200 nm – 310 nm and
154   Tungsten source was used for the range 310 nm – 800 nm. The angle of incidence and angle of
155   reflection were set to 5° throughout the experiment. The equipment used a photomultiplier tube

156   (PMT) detector. The reflectance from a surface is evaluated by its refractive index profile[6]. In
157   general, a flat surface has a high reflectance due to the discontinuous refractive index profile, whereas
158   structured surface suppresses reflection with its graded refractive index profile[6].

159   **3. Results and Discussion**

160   Figure 1 shows the SEM images of densely packed urchins after growth in 5 mM zincate solution on
161   a seeded silicon substrate (Figure S2) at ~20° C for 12 h, and the simple fabrication method is
162   described in Figure S1. XRD (Figure S11) confirmed that these urchins were ZnO. The morphology
163   of an individual urchin (Figure 1c) reveals sharply tapered needles radiating from the centre. The
164   length of the needles was L~ 1.65 ±0.11 µm, its width at the central base D_c ~ 156±24 nm and at the
165   tip D_t ~ 13±7 nm, with a tapering angle θ ~10° and an average tip-to-tip spacing s ~ 504±119 nm
166   (see Figure S3- S5 for the size distribution analysis).
167   Previously, ZnO nano- and micro-structures bearing resemblance of the urchin morphology have
168   been reported. For instance, Elias et al.[50] prepared µm-sized hollow spheres with a ZnO nano-
169   columns coating using atom layer deposition and electrodeposition, whilst the method by Shen et
170   al.[49] used thermos-evaporation of metallic Zn powder at high temperature (~750° C).   Wahab et
171   al.[45] fabricated ZnO nano-flowers blunt tapering via pH-controlled reactions in solution of zinc
172   acetate dihydrate and sodium hydroxide at 90° C. Using a similar approach, Gokarna et al.[46]
173   synthesised ZnO urchin-like structures with columnar nanoneedles.   Hieu et al.[47] sputtered zinc
174   onto a polystyrene-sphere array and subsequent oxidation at 500° C led to columnar ZnO urchins ;
175   and the method by Taheri et al.[48] also involved depositing zinc acetate dihydrate precursor
176   followed by calcination at 500° C.   The solution synthesis method we report here is relatively much
177   simpler (at RT and applicable to different surfaces as we show below) compared to these previous
178   studies, producing spiky tapered morphology of the urchin needles with a very high density
179   previously unreported. The presence of high-density spiky ZnO urchins endows the surface with
180   multi-functionalities as discussed below.
181   SEM images of the region not covered by the urchins reveal vertical ZnO nanoneedles (from the
182   primary growth step as referred to in Figure 1d, g) with an average base diameter ~ 90±20 nm,
183   smaller than that of the urchin needles (Figure 1d-g), and the cross-section SEM view confirms that
184   the ZnO urchins were formed atop a layer of nanoneedle arrays (Figure 1a, b). Orthorhombic ε-
185   $Zn(OH)_2$ crystals with facet edges ~10-30 µm were also observed (Figure S7), with ZnO urchins (the
186   secondary growth in Figure 1d) decorating the facets. The tapered or spiky nanoneedle geometry
187   might be attributed to the concentration gradient of the zinc ions in the vicinity of the substrate where
188   the ZnO nanocrystal seeds provided the nucleation sites for ZnO nanoneedles growth (Figure 1f,
189   g)[61].
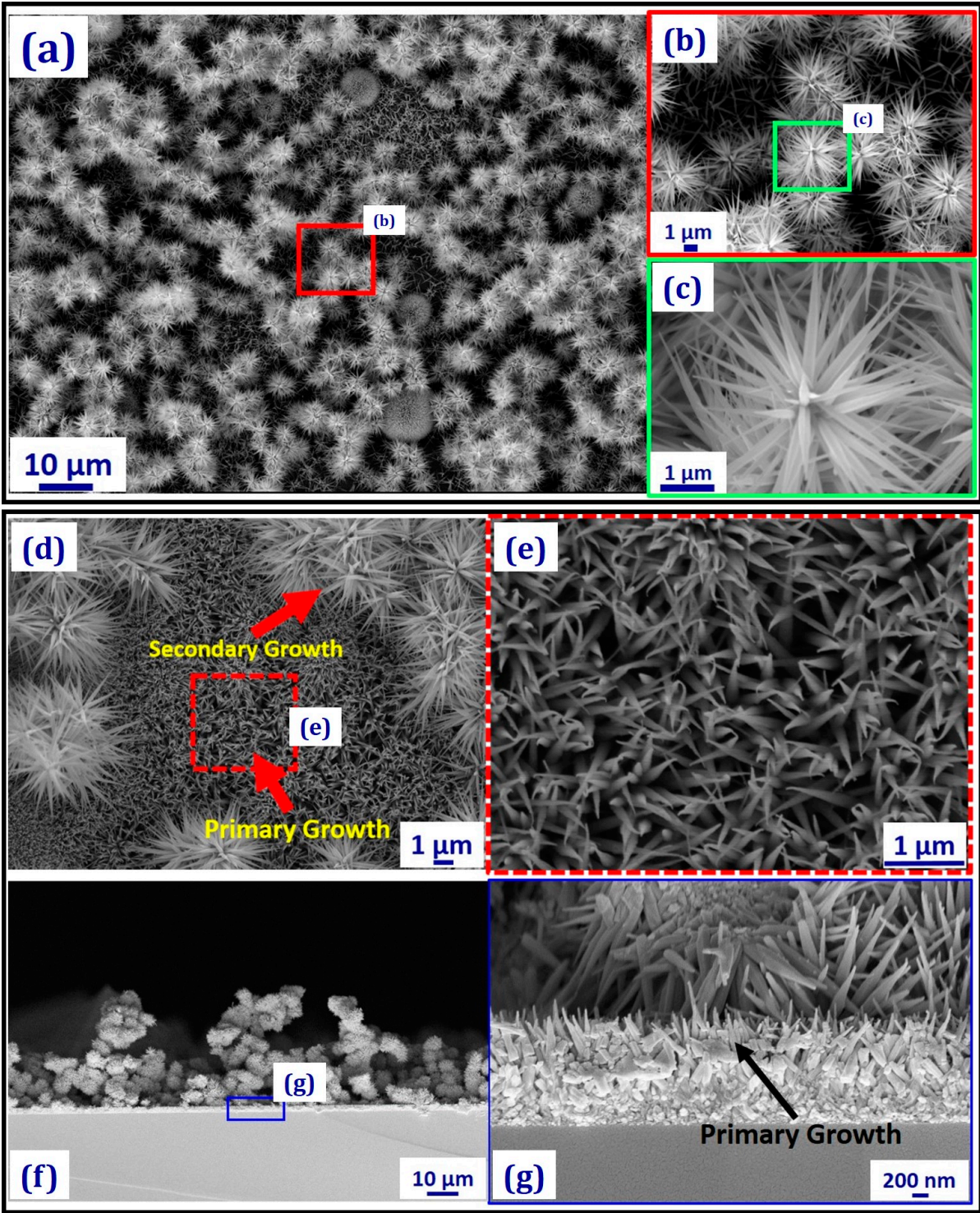
Figure 1: (a) Scanning electron microscopy (SEM) images of ZnO urchins on a seeded silicon substrate; (b) SEM images depicting the ZnO urchin and primary vertical nanoneedle growth on the silicon substrate. SEM images show random multidirectional growth of the nanoneedles comprising the urchin (seeding concentration of zinc acetate dihydrate - 5 mM, synthesis time for ZnO urchin growth - 12 h, and temperature - 20°C).

To understand the growth kinetics of the ZnO nanostructures, SEM images (Figure 2, Figure S8 and S9) of the seeded silicon substrates were taken at different growth time intervals t. At $t = 0.5$-1 h (Figure 2a, b), only the primary growth of vertical nanoneedle structures was observed. At $t = 3$ h, the

200   secondary growth of urchin-like structures atop the nanoneedle array with a diameter ϕ ~1μm was
201   observed. The density and size of the urchins and length of the urchin needle L then increased with
202   time (see Figure S5 for urchin needle length L *vs.* growth time t), whilst the tapering angle remained
203   largely constant at θ ~10°. Figure 2g presents the GIXRD data (see section II.4. in supplementary
204   information) on the seeded silicon substrates at different growth time intervals. The intense (002)
205   ZnO peak at $t < 3$h is consistent with the primary growth of vertical ZnO nanoneedles. The ε-Zn(OH)$_2$
206   phase (orthorhombic crystals) is visible for the samples with reaction time $t > 3$ h (Figure 2g). This
207   shows that the ZnO nanoneedles started forming after 30 min and Zn(OH)$_2$ crystals after 3 h, likely
208   together with the secondary growth of ZnO urchins (Figure 2c-f).
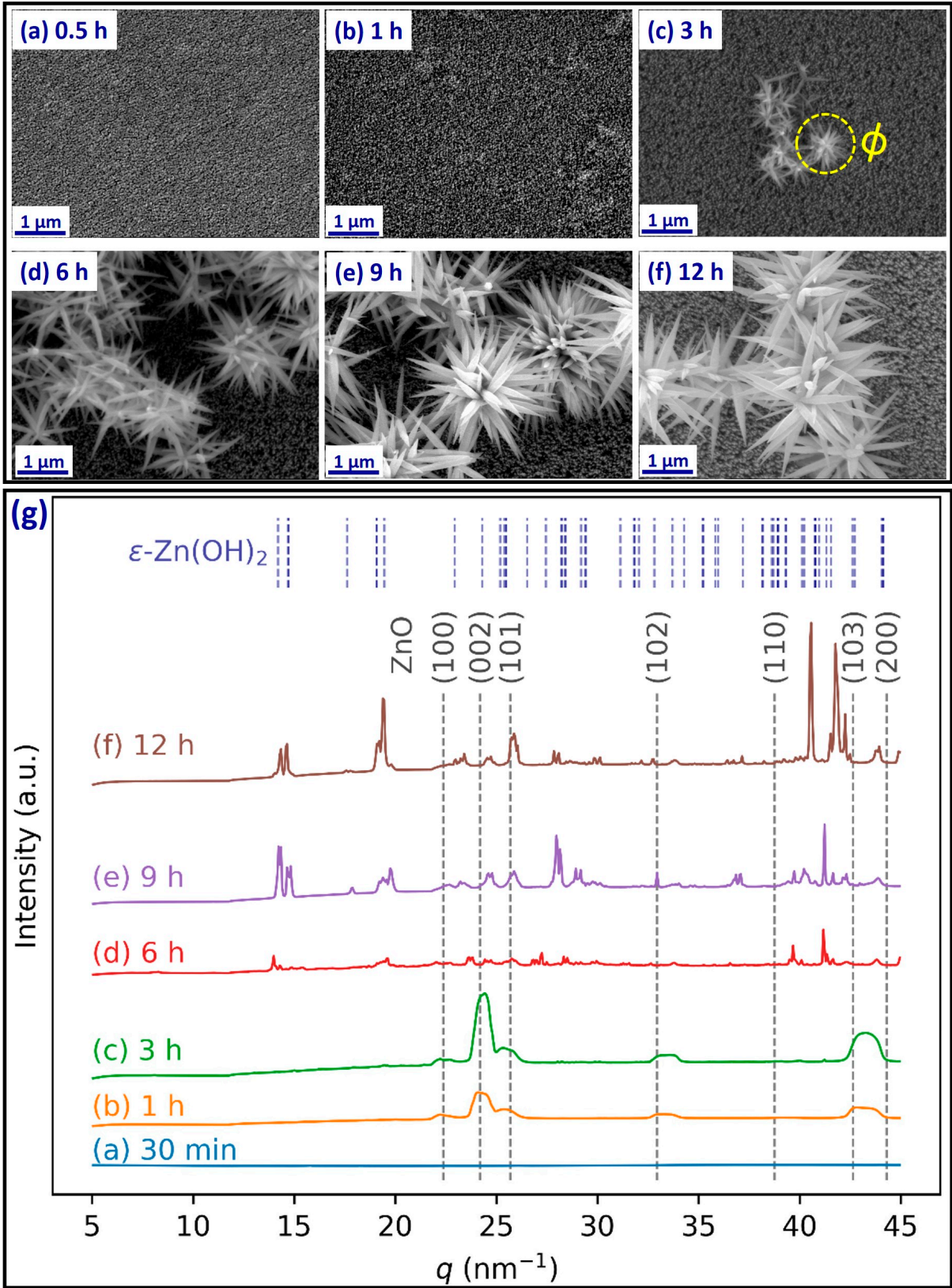
Figure 2: (a-f) SEM images of seeded silicon substrates in 5 mM zincate growth solution at different growth time intervals t = 0.5 – 12 h; and (g) corresponding GIXRD data for the substrates.

To evaluate the effect of substrate seeding on the ZnO urchin morphology, the one-step fabrication procedure was performed using unseeded silicon substrates (i.e. in 5 mM zincate solution at 20° C, and 12 h growth time). SEM image in Figure 3a shows that urchin like ZnO nanostructures were also

215   obtained with a high surface coverage (Figure 3a, c), with urchins found on orthorhombic ε-Zn(OH)$_2$
216   crystal facets (Figure 3b). There was no significant difference in the urchin morphology (urchin size
217   ϕ, needle length L, diameter D, and tip angle θ) compared to the seeded substrate. However, some
218   urchins in the bare silicon area had a smaller number of nanoneedles (Figure 3d). Comparison of the
219   XRD patterns in Figure S11 for the 12 h growth shows that, on the unseeded Si sample, the most
220   intense peaks correspond to the ε-Zn(OH)$_2$ crystal structure, consistent with the SEM images shown
221   in Figure 3.
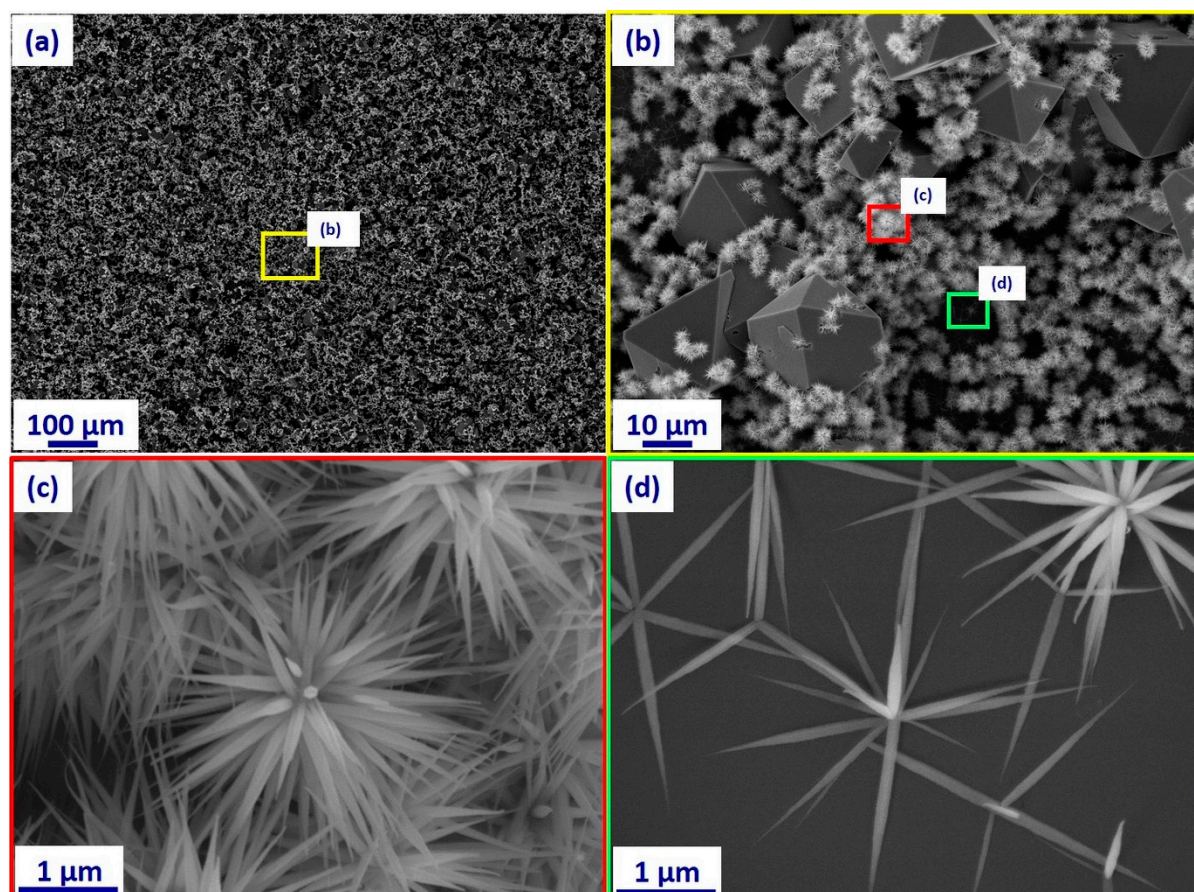
222
223   Figure 3: SEM images of ZnO nanostructures grown on the unseeded silicon substrate in the one-step
224   synthesis (12 h, 20° C), with a high coverage of ZnO urchins (a) with morphology similar to that on
225   seeded Si substrates (b, c). Orthorhombic ε-Zn(OH)$_2$ crystals were also observed (b) decorated with
226   urchins. Urchins with a smaller number of needles were also observed in the bare silicon area (d).
227
228   Time dependent growth of ZnO urchins on non-seeded silicon substrate was also studied, and SEM
229   images at different growth time intervals are shown in Figure S10. Similar to the seeded Si substrates,
230   ZnO urchins emerged between 1-3 h of the growth time (Figure S10a, e), and their dimensions and
231   surface coverage increased with time (Figure S10), with orthorhombic ε-Zn(OH)$_2$ crystals starting to
232   appear on the surface between 3-6 h of the synthesis (Figure S10b).
233   Figure   further compares the XRD on both seeded and non-seeded silicon substrates after the growth
234   in the zincate solution for 12 h. Peaks corresponding to both ZnO (PDF 36-1451) and ε-Zn(OH)$_2$ (PDF
235   38-385) were identified, confirming their formation on the surfaces. The most intense peak in the
236   seeded silicon sample corresponds to the ZnO (002) plane, which is the preferential growth direction
237   of ZnO nanoneedles[62]. Along with the SEM images, this confirms that on seeded Si the primary

238   growth led to ZnO nanoneedles, with the ZnO urchins grown atop in the secondary growth stage. In
239   the case of the unseeded Si sample, the most intense peaks correspond to the ε-Zn(OH)$_2$ crystal
240   structure. This is consistent with the SEM image (Figure 3b) which shows that the substrate was
241   covered by ZnO urchins grown on orthorhombic Zn(OH)$_2$ crystals and bare Si surface, with a
242   significantly smaller amount of arrayed ZnO nanoneedles (Figure 3d).
243   Growth of the ZnO nanoneedles and urchin structures were also trialled on copper sheets, soft PDMS
244   and transparent glass substrates, all seeded by dipping the substrates in a solution of zinc acetate
245   dihydrate in ethanol (Figure S1). The ZnO nanostructures grown on these surfaces (Figure4g-i)
246   exhibited similar urchin morphologies to the those on silicon substrates (Figure 1). The growth on
247   glass was also evident, as it became translucent after the growth (Figure4d and Figure S12). This
248   demonstrates that the facile, room temperature synthesis method for ZnO nanoneedles and urchins
249   is adaptable to various substrates.
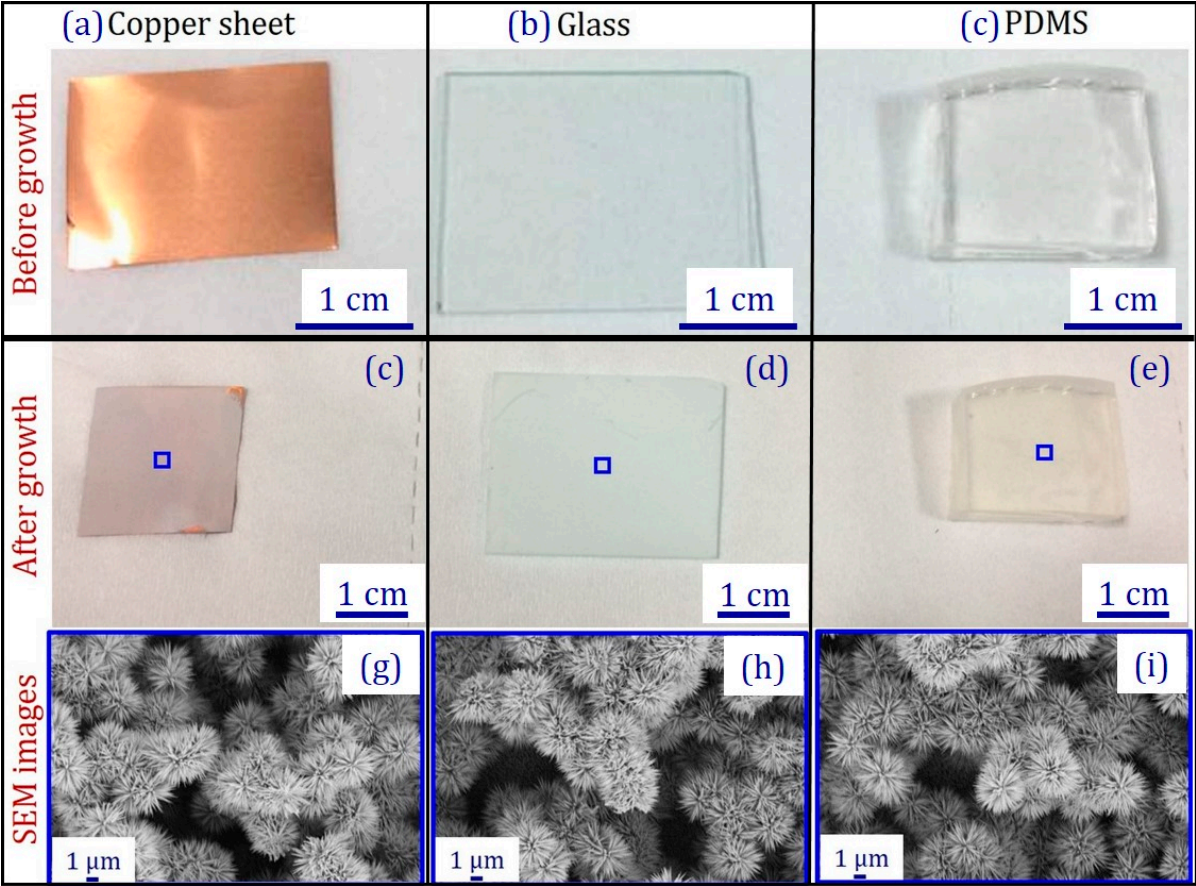
251   Figure 4: (a) Growth of ZnO urchin on seeded copper, glass slide and PDMS surfaces and the
252   corresponding SEM images of the ZnO urchin formed on the substrates.
253
254   Si surfaces with ZnO urchins (both seeded and unseeded, 12 h growth time) were superhydrophilic,
255   with a water droplet placed on these surfaces spreading completely and showing a water contact
256   angle $\theta \sim 0°$ (Table S1). They became superhydrophobic after overnight silanization (Table S1)
257   with apparent water contact angle $\theta \sim 159°\pm1.4°$ (Figure 5a) and a contact angle hysteresis $\Delta\theta < 7°$
258   was observed. Water droplet exhibited Cassie-Baxter state on the silanized ZnO urchin surface,
259   which is evident from the high contact angle and low contact angle hysteresis. For comparison, Table

260   S1 shows that bare Si and Si coated with 20 nm ZnO thin film exhibited hydrophilic behaviour with
261   apparent water contact angle $\theta \sim 36°$ and $\sim 61°$, respectively.

262   To further demonstrate the superhydrophobicity in dynamic conditions, a 10 µL water droplet was
263   allowed to fall on the silanized ZnO urchin surface from a height of 7 cm with a *Weber number* $We =$
264    $\frac{\rho V^2 D_w}{\gamma} = 49$, where $\rho = 1$ g cm^{-3} is the density of water, $V = \sqrt{2gh}$=1.17 m s^{-1} the impact velocity of the
265   falling droplet, γ = 73.8 mN m^{-1} the surface tension of water, and D_w = 2.67 mm the diameter of
266   droplet (Table S1). The dynamic process was captured using a high-speed camera with a 10,000-fps
267   capture rate. The water droplet bounced off the superhydrophic surface completely without leaving
268   any visible residues, with a droplet-substrate contact time of 15.3 ms (Figure 5b and Video S1) which
269   is close to the theoretical contact time (($\frac{\rho D_w^3}{\gamma}$)$^{1/2}$ = 16.25 ms) for water droplet on superhydrophobic
270   surface[63].
271   In addition, the ZnO urchin coated surface also demonstrated anti-reflective behaviour. **Error!**
272   **Reference source not found.**c shows <1% reflectance (R) over the wavelength range λ = 200-800 nm
273   on the urchin surface, compared to two control samples (bare Si and Si with 20 nm ZnO thin film).
274   There have been previous reports on fabrication of nanostructured anti-reflective surfaces [6,11,64–
275   70]. Different techniques such as dry etching, wet etching, metal assisted etching, nanoimprint
276   lithography, etching using O$_2$ plasma and inductively coupled plasma, optical lithography followed
277   by etching etc.[71] have been used to fabricate such surfaces on silicon, polymers, and glass to achieve
278   low reflectance. In comparison, the fabrication method we used to achieve the low reflectance (R <
279   1%) was simple with the synthesis undertaken at room temperature without the need for
280   sophisticated instrumentation.
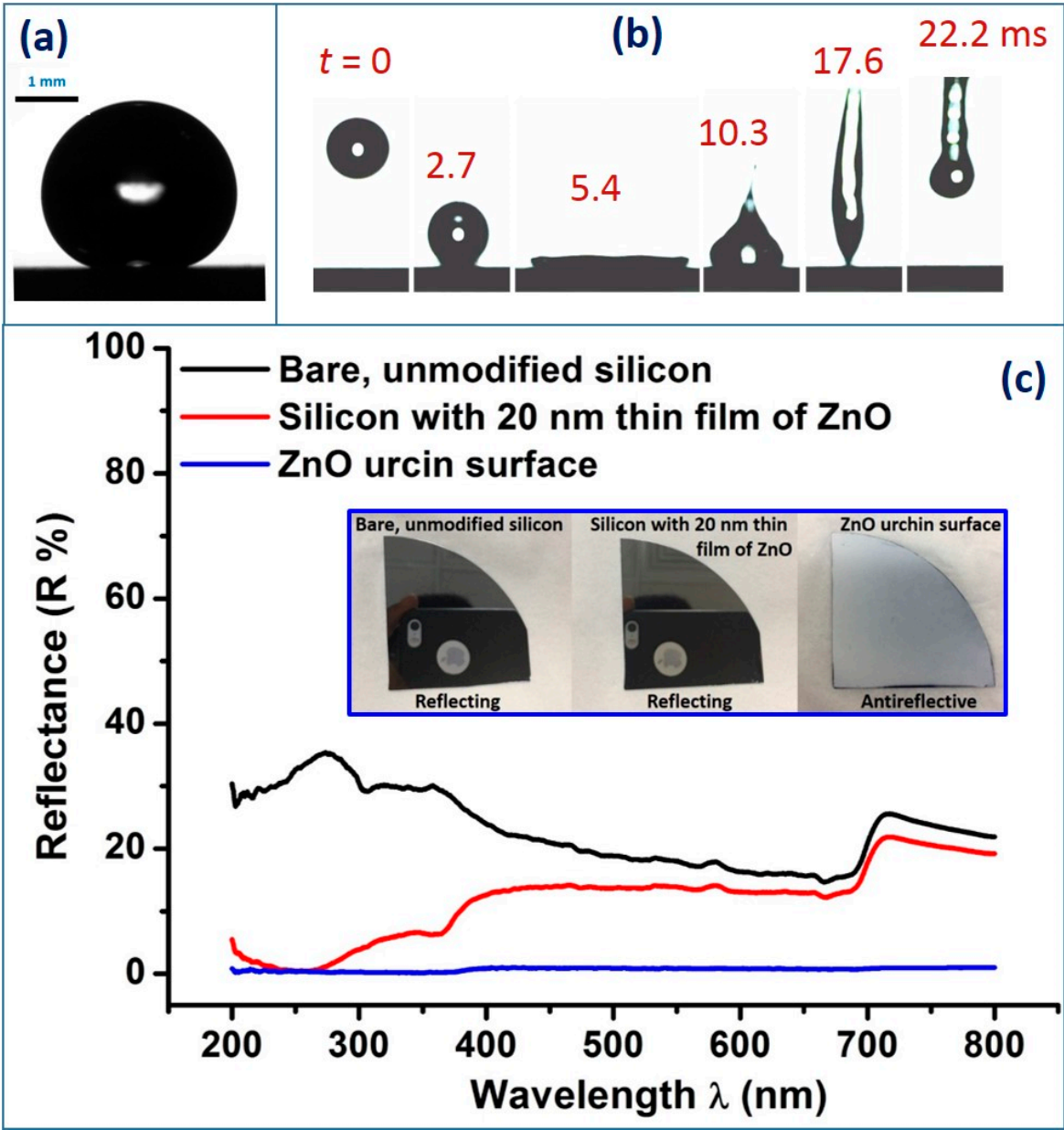
Figure 5: (a) Photograph of a 10 μL water droplet on ZnO urchin-coated surface after silanization, with a contact angle $\theta \sim 159°\pm1.4°$. Prior to silanization, the surface was highly hydrophilic, displaying complete wetting by water with $\theta \sim 0°$ (Table S1).   (b) High-speed camera images of a 10 μL droplet bouncing off the superhydrophobic ZnO urchin surface, with a contact time of 15.3 ms. (c) Reflectance from the ZnO urchin surface compared to the two control surfaces in the wavelength range $\lambda= 200 – 800$ nm. ZnO urchin surface was found to be the most anti-reflective with reflectance $R < 1\%$ over the whole wavelength range. The inset shows the highly reflective bare Si and Si with 20 nm ZnO film (with the reflection of the iPhone used to take the photo clearly visible), in contrast to the anti-reflective characteristic of the ZnO urchin surface.

To evaluate the bacterial interaction with the fabricated ZnO urchins on the seeded Si surface, it was submerged in 2 mL *E. coli* culture in phosphate-buffered saline (PBS) for 24 h and then imaged with SEM. This was compared with two control samples: unmodified bare Si and Si with a 20 nm sputtered ZnO film (Figure S13). SEM images in Error! Reference source not found.a (see also Table S2) show

296 bacteria growth on the control surfaces; in contrast, no bacterium was observed on the ZnO
297 nanostructured surface (Figure 6c, d). In addition, the SEM analysis revealed a change in the
298 morphology of the ZnO urchins (inset in **Error! Reference source not found.**c): after 24 h immersion
299 in the _E. coli_ culture, the spiky urchin structure was transformed into the hexagonal pyramid structure
300 (see Figure S14a). This can be attributed to the formation of sodium zinc phosphate hydrate (NaZn-
301 PO$_4$.H$_2$O)[72] due to the reaction between ZnO urchins and the PBS (_cf._ XRD data in Figure S14b).
302 ZnO is known to exhibit antimicrobial efficacy[15–19], killing bacteria and prohibiting bacterial
303 growth on its surface _via_ release of Zn^{2+} ions which solicits generation of reactive oxygen species
304 (ROS). A number of naturally occurring surfaces bearing spiky nanotextures (e.g. cicada wing,
305 dragonfly wing, and gecko skin) have been reported to exhibit bactericidal efficacy, attributed to
306 puncturing or stretching of the bacterial membrane, although the detailed mechanisms remain to be
307 fully understood[3,11,73–76]. Hence, we suggest that the ZnO urchin surfaces could prevent bacterial
308 growth by combining synergistically the inherent chemical activity of ZnO and the spiky morphology
309 of the urchins that inhibits the bacteria to colonise on the surface of the ZnO urchins[18,77–79]. The
310 sharp topography of the nanoneedles are particularly effective in disrupting the bacterial cell wall by
311 imparting the localised stress on the bacterial membrane[80]. There are previous reports on reduced
312 bacterial adhesion on superhydrophobic surfaces[81–84] where the antiwetting property of the
313 surface plays a crucial role in the interaction of the bacteria with the surface; whereas our fabricated
314 ZnO urchin surfaces exhibited bacteriophobic behaviour in a hydrophilic state (with a water contact
315 angle $\theta \sim 0^\circ$).
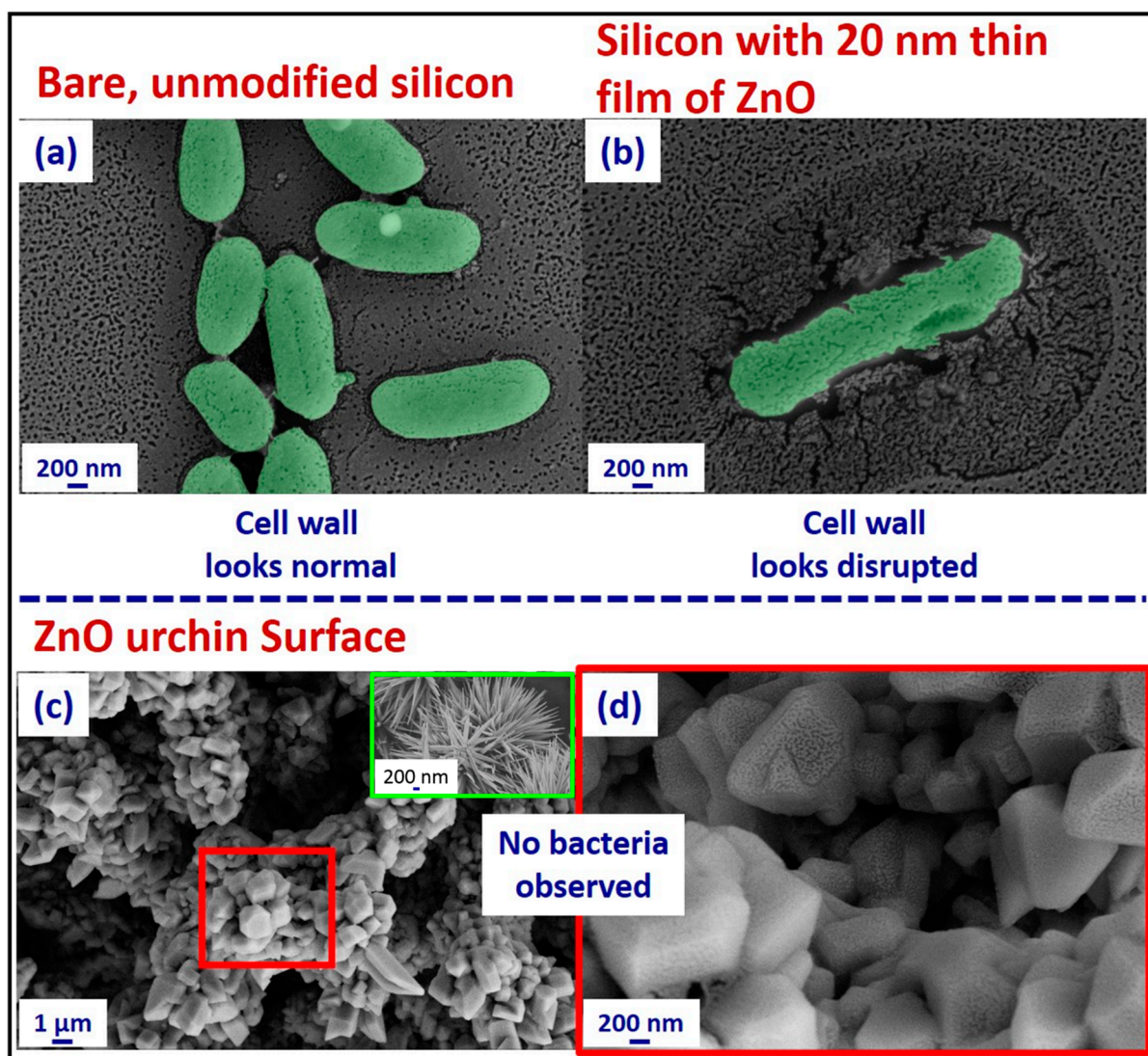
Figure 6: Representative SEM images of *E. coli* (false coloured Green) on different surfaces after 24 h of bacterial culture. (a) bare, unmodified silicon, (b) silicon with 20 nm thin film of ZnO and (c) & (d) ZnO urchin surface. Inset in Figure 6(c) shows the morphology of the ZnO urchin before bacterial culture on the urchin surface.

5. Conclusions

In summary, ZnO urchin structures were fabricated via a simple method involving submergence of a substrate (Si, PDMS, glass, or Cu) in an alkaline aqueous zincate ion ($Zn(OH)_4^{2-}$) solution at room temperature (~20° C). On the Si substrate seeded with ZnO nanocrystals, we observed ZnO urchin structures atop vertically aligned ZnO nanoneedles. The urchins consisted of densely packed, µm-long spiky ZnO nanoneedles radiating from the urchin centre, with a tapering angle of ~10°. The growth kinetics of the ZnO surface nanostructures was studied by time resolved SEM, revealing that the urchin morphology emerged at ~ 3 h reaction time with a small number of, but tapered, nanoneedles. The nanoneedle density and length then progressively increased with the reaction time. On the seeded Si substrate, a primary growth step of the vertical ZnO nanoneedles was identified preceding the secondary urchin growth. The ZnO urchin coated surface exhibited anti-reflective properties, reducing the reflectance to less than 1%. It was highly hydrophilic, with a water contact

333   angle of ~0°; after silanization, it exhibited superhydrophobicity with a water contact angle of 159°
334   and hysteresis smaller than 7°. In addition, its dynamic hydrophobicity was demonstrated by
335   bouncing-off of a water drop as captured by a high-speed camera, with resident time of 15.9 ms.
336   Furthermore, the ZnO urchin surface showed bacteriophobic behaviour, as compared to the control
337   Si and ZnO-coated surfaces, with no bacterium colonization observed on the surface after 24 h
338   incubation in *E. coli*. The facile method for preparing ZnO urchins with unique morphology of
339   tapered nanoneedles, and its ready adaptability to different surfaces (including polymers), may open
340   new routes for fabrication of multifunctional ZnO nanostructured surfaces.

341

342   **Supplementary Materials:** The following are available online,
343   **Figure S1:** Process flow of the fabrication of ZnO nanostructures on seeded silicon substrates at near room
344   temperature, **Figure S2:** SEM images of a silicon substrate seeded with ZnO nanoislands in 5 mM zinc acetate
345   dihydrate solution (dipping × 5 times and annealed at 300° C for 30 minutes), **Figure S3:** Nanoneedle dimension
346   measurement using ImageJ software. The values in the main text were averaged from 50 different needles, with
347   the measurements of different parameters at each single needle repeated 5 times, **Figure S4:** Size distribution
348   from ImageJ analysis of the nanoneedle tip diameter at the top D_t urchins ranging from 7-30 nm with an average
349   diameter of D_t = 13±7 nm, **Figure S5:** Length of the nanoneedles L in the urchin structure vs. growth time. Length
350   of the nanoneedle was found to increase with respect to synthesis time. Stars in figure shows that for time points
351   0, 0.5 and 1 h there was no formation of urchin structures, **Figure S6:** (a) the angled view after 9 h growth,
352   showing ZnO urchins on the top of highly (b) oriented ZnO nanoneedles, **Figure S7:** Representative FESEM
353   images of the seeded silicon substrate post 12 h synthesis in the zincate solution, **Figure S8:** SEM images of
354   seeded silicon substrates after growth in zincate solution at different time intervals. Density of ZnO nano urchins
355   was found to increase with the increase synthesis time, **Figure S9:** SEM images of seeded silicon substrates after
356   growth in zincate solution at different time intervals. $Zn(OH)_2$ crystals were observed on the substrates for
357   synthesis time t > 3 h, **Figure S10:** SEM images of ZnO urchins on a non-seeded silicon substrate, taken at
358   different time intervals: (a) 3 h, (b) 6 h, (c) 9 h, and (d) 12 h. (e-h) show enlarged views of the square regions as
359   labelled in (a-d), respectively, **Figure S11:** XRD of (a)&(b) seeded and (c)&(d) unseeded silicon substrates after
360   growth in the zincate solution at 20° C for 12 h, with the ZnO and ε-$Zn(OH)_2$ peaks indicated by * and ▼,
361   respectively, and the enlarged views shown on the right-hand side, **Figure S12:** Optical image showing the loss
362   in transparency after the formation of ZnO urchin/nanoneedles on the glass substrate, **Figure S13:** 12 well culture
363   plate for pouring the bacterial suspension on different samples, **Figure S14:** (a) SEM and (b) XRD of ZnO
364   nanourchin surface after pouring the bacterial culture for 24 hours. Formation of sodium zinc phosphate hydrate
365   ($NaZn$-$PO_4.H_2O$) was observed on the surface due to the reaction of ZnO with PBS leading to the change in
366   morphology of the spiky ZnO nanowires, **Table S1:** Apparent contact angles of DI water droplet on different
367   substrates, **Table S2:** SEM of *E. coli* on different substrates, **Video S1:** Superhydrophobic ZnO urchin.

368

369   **Author Contributions:** AT and WHB conceived and designed experiments; AT and PW synthesised and
370   characterised ZnO urchins; AT, SS, DN and PS performed experiments on anti-reflectivity, *E coli* colonisation,
371   and dynamic superhydrophobicity of the urchin surfaces; PW, OB and WHB performed synchrotron XRD
372   measurements. All authors contributed to data analysis and the manuscript writing.

373

374   **Acknowledgments:** AT acknowledges the funding from the British Council, United Kingdom and Department
375   of Biotechnology, Government of India through the Newton-Bhabha PhD fellowship program. PW
376   acknowledges the funding from the UK Engineering and Physical Sciences Research Council (EPSRC) through

Peer-reviewed version available at *Colloids Interfaces* **2018**, *2*, 74; <u>doi:10.3390/colloids2040074</u>

377   the Bristol Centre for Functional Nanomaterials (BCFN, grant no. EP/G036780/1). PS would like to thank the

378   Ministry of Electronics and Information Technology, Government of India for the financial support. DPN

379   acknowledges the funding by the Department of Biotechnology-Indian Institute of Science partnership program.

380   W.H.B. would like to acknowledge funding from the EPSRC (EP/H034862/1 and Building Global Engagement

381   in Research (BGER)), European Cooperation in Science and Technology (CMST COST) Action CM1101

382   "Colloidal Aspects of Nanoscience for Innovative Processes and Materials", and Marie Curie Initial Training

383   Network (MCITN) on "Soft, Small, and Smart: Design, Assembly, and Dynamics of Novel Nanoparticles for

384   Novel Industrial Applications" (NanoS3; FP7 Grant No. 290251). We acknowledge the beamline BM28 at the

385   European Synchrotron Radiation Facility (a UK EPSRC funded facility) for beam time and the staff there for their

386   help.

387   **Conflicts of Interest:** The authors declare no conflict of interest

References

389   1.   Tang, P.; Zhang, W.; Wang, Y.; Zhang, B.; Wang, H.; Lin, C.; Zhang, L. Effect of Superhydrophobic
390   Surface of Titanium on Staphylococcus aureus Adhesion. *J. Nanomater.* **2011**, *2011*, 1–8.

391   2.   Fadeeva, E.; Truong, V.K.; Stiesch, M.; Chichkov, B.N.; Crawford, R.J.; Wang, J.; Ivanova, E.P. Bacterial
392   retention on superhydrophobic titanium surfaces fabricated by femtosecond laser ablation. *Langmuir*
393   **2011**, *27*, 3012–3019.

394   3.   Ivanova, E.P.; Hasan, J.; Webb, H.K.; Truong, V.K.; Watson, G.S.; Watson, J.A.; Baulin, V.A.; Pogodin, S.;
395   Wang, J.Y.; Tobin, M.J.; et al. Natural Bactericidal Surfaces: Mechanical Rupture of Pseudomonas
396   aeruginosa Cells by Cicada Wings. *Small* **2012**, *8*, 2489–2494.

397   4.   Pogodin, S.; Hasan, J.; Baulin, V.A.; Webb, H.K.; Truong, V.K.; Phong Nguyen, T.H.; Boshkovikj, V.;
398   Fluke, C.J.; Watson, G.S.; Watson, J.A.; et al. Biophysical Model of Bacterial Cell Interactions with
399   Nanopatterned Cicada Wing Surfaces. *Biophys. J.* **2013**, *104*, 835–840.

400   5.   Yao, C.; Webster, T.J.; Hedrick, M. Decreased bacteria density on nanostructured polyurethane. *J. Biomed.*
401   *Mater. Res. - Part A* **2014**, *102*, 1823–1828.

402   6.   Chattopadhyay, S.; Huang, Y.F.; Jen, Y.J.; Ganguly, A.; Chen, K.H.; Chen, L.C. Anti-reflecting and
403   photonic nanostructures. *Mater. Sci. Eng. R Reports* **2010**, *69*, 1–35.

404   7.   Yamada, N.; Kim, O.N.; Tokimitsu, T.; Nakai, Y.; Masuda, H. Optimization of anti-reflection moth-eye
405   structures for use in crystalline silicon solar cells. *Prog. Photovoltaics Res. Appl.* **2011**, *19*, 134–140.

406   8.   Park, H.; Shin, D.; Kang, G.; Baek, S.; Kim, K.; Padilla, W.J. Broadband optical antireflection enhancement
407   by integrating antireflective nanoislands with silicon nanoconical-frustum arrays. *Adv. Mater.* **2011**, *23*,
408   5796–5800.

409   9.   Park, K.-C.; Choi, H.J.; Chang, C.-H.; Cohen, R.E.; McKinley, G.H.; Barbastathis, G. Nanotextured Silica
410   Surfaces with Robust Superhydrophobicity and Omnidirectional Broadband Supertransmissivity. *ACS*
411   *Nano* **2012**, *6*, 3789–3799.

412   10.   Zhang, D.; Yu, W.; Hao, D.; Li, L.; Liu, H.; Lu, Z. Functional nanostructured surfaces in hybrid sol–gel
413   glass in large area for antireflective and super-hydrophobic purposes. *J. Mater. Chem.* **2012**, *22*, 17328.

414   11.   Tripathy, A.; Sreedharan, S.; Bhaskarla, C.; Majumdar, S.; Peneti, S.K.; Nandi, D.; Sen, P. Enhancing the
415   Bactericidal Efficacy of Nanostructured Multifunctional Surface Using an Ultrathin Metal Coating.
416   *Langmuir* **2017**, *33*, 12569–12579.

417   12.   Zhang, Y.; Ram, M.K.; Stefanakos, E.K.; Goswami, D.Y. Synthesis, characterization, and applications of
418   ZnO nanowires. *J. Nanomater.* **2012**, *2012*.

419   13.   Jones, F.; Tran, H.; Lindberg, D.; Zhao, L.; Hupa, M. Thermal stability of zinc compounds. *Energy and*
420   *Fuels* **2013**, *27*, 5663–5669.

421   14.   Makarona, E.; Athanassiou, B.; Prionistis, C.; Tegou, E.; Tsamis, C. A cost-efficient solution-based
422   process for the development of ZnO nanostructures: A comprehensive study of the role of the seeding
423   layer formation conditions. *Procedia Eng.* **2015**, *120*, 447–450.

424   15.   Kumar, R.; Umar, A.; Kumar, G.; Nalwa, H.S. Antimicrobial properties of ZnO nanomaterials: A review.
425   *Ceram. Int.* **2017**, *43*, 3940–3961.

426   16.   Xie, Y.; He, Y.; Irwin, P.L.; Jin, T.; Shi, X. Antibacterial activity and mechanism of action of zinc oxide
427   nanoparticles against Campylobacter jejuni. *Appl. Environ. Microbiol.* **2011**, *77*, 2325–2331.

428   17.   Sirelkhatim, A.; Mahmud, S.; Seeni, A.; Kaus, N.H.M.; Ann, L.C.; Bakhori, S.K.M.; Hasan, H.; Mohamad,
429   D. Review on zinc oxide nanoparticles: Antibacterial activity and toxicity mechanism. *Nano-Micro Lett.*
430   **2015**, *7*, 219–242.

431   18.   Tam, K.H.; Djurišić, A.B.; Chan, C.M.N.; Xi, Y.Y.; Tse, C.W.; Leung, Y.H.; Chan, W.K.; Leung, F.C.C.; Au,
432   D.W.T. Antibacterial activity of ZnO nanorods prepared by a hydrothermal method. *Thin Solid Films*
433   **2008**, *516*, 6167–6174.

434   19.   Abinaya, C.; Mayandi, J.; Osborne, J.; Frost, M.; Ekstrum, C.; Pearce, J.M. Inhibition of growth of S .
435   epidermidis by hydrothermally synthesized ZnO nanoplates. *Mater. Res. Express.* **2017**, 4, 075401.

436   20.   Li, Z.; Yang, R.; Yu, M.; Bai, F.; Li, C.; Wang, Z.L.; Li, Z.; Yang, R.; Yu, M.; Bai, F.; et al. Cellular Level
437   Biocompatibility and Biosafety of ZnO Nanowires Cellular Level Biocompatibility and Biosafety of ZnO
438   Nanowires. **2008**, *112*, 20114–20117.

439   21.   Li, P.; Liu, H.; Lu, B.; Wei, Y. Formation mechanism of 1D ZnO nanowhiskers in aqueous solution. *J.*
440   *Phys. Chem. C* **2010**, *114*, 21132–21137.

441   22.   McBride, R. a.; Kelly, J.M.; McCormack, D.E. Growth of well-defined ZnO microparticles by hydroxide
442   ion hydrolysis of zinc salts. *J. Mater. Chem.* **2003**, *13*, 1196–1201.

443   23.   Wang, J.; Hou, S.; Zhang, L.; Chen, J.; Xiang, L. Ultra-rapid formation of ZnO hierarchical structures
444   from dilution-induced supersaturated solutions. *CrystEngComm* **2014**, *16*, 7115.

445   24.   You, T.; Yan, J.; Zhang, Z.; Li, J.; Tian, J.; Yun, J.; Zhao, W. Fabrication and optical properties of needle-
446   like ZnO array by a simple hydrothermal process. *Mater. Lett.* **2012**, *66*, 246–249.

447   25.   Safa, S. Enhanced UV-detection properties of carbon nanotube impregnated ZnO nanourchins. *Optik*
448   *(Stuttg).* **2015**, *126*, 2194–2198.

449   26.   Ko, Y.H.; Yu, J.S. Tunable growth of urchin-shaped ZnO nanostructures on patterned transparent
450   substrates. *CrystEngComm* **2012**, *14*, 5824.

451   27.   Imani, R.; Drašler, B.; Kononenko, V.; Romih, T.; Eleršič, K.; Jelenc, J.; Junkar, I.; Remškar, M.; Drobne,
452   D.; Kralj-Iglič, V.; et al. Growth of a Novel Nanostructured ZnO Urchin: Control of Cytotoxicity and
453   Dissolution of the ZnO Urchin. *Nanoscale Res. Lett.* **2015**, *10*, 1–10.

454   28.   Banerjee, D.; Lao, J.Y.; Wang, D.Z.; Huang, J.Y.; Steeves, D.; Kimball, B.; Ren, Z.F. Synthesis and
455   photoluminescence studies on ZnO nanowires. *Nanotechnology* **2004**, *15*, 404–409.

456   29.   Wasik, P.; Redeker, C.; Dane, T.G.; Seddon, A.M.; Wu, H.; Briscoe, W.H. Hierarchical Surface Patterns
457   upon Evaporation of a ZnO Nanofluid Droplet: Effect of Particle Morphology. *Langmuir* **2018**, *34*, 1645–
458   1654.

459   30.   Wu, H.; Chen, L.X.; Zeng, X.Q.; Ren, T.H.; Briscoe, W.H. Self-assembly in an evaporating nanofluid
460   droplet: rapid transformation of nanorods into 3D fibre network structures. *Soft Matter* **2014**, *10*, 5243–
461   5248.

31. Greene, L.E.; Law, M.; Tan, D.H.; Montano, M.; Goldberger, J.; Somorjai, G.; Yang, P. General route to vertical ZnO nanowire arrays using textured ZnO seeds. *Nano Lett.* **2005**, *5*, 1231–1236.

32. Wang, G.; Li, Z.; Li, M.; Feng, Y.; Li, W.; Lv, S.; Liao, J. Synthesizing vertical porous ZnO nanowires arrays on Si/ITO substrate for enhanced photocatalysis. *Ceram. Int.* **2018**, *44*, 1291–1295.

33. Gacusan, J.; Kobayashi, N.P.; Sanghadasa, M.; Meyyappan, M. Controlled growth of vertical ZnO nanowires on copper substrate. *Appl. Phys. Lett.* **2013**, *083105*.

34. Wu, C.; Shen, L.; Yu, H.; Huang, Q.; Zhang, Y.C. Synthesis of Sn-doped ZnO nanorods and their photocatalytic properties. *Mater. Res. Bull.* **2011**, *46*, 1107–1112.

35. Solís-Pomar, F.; Martínez, E.; Meléndrez, M.F.; Pérez-Tijerina, E. Growth of vertically aligned ZnO nanorods using textured ZnO films. *Nanoscale Res. Lett.* **2011**, *6*, 524.

36. Gurav, A.B.; Latthe, S.S.; Vhatkar, R.S.; Lee, J.G.; Kim, D.Y.; Park, J.J.; Yoon, S.S. Superhydrophobic surface decorated with vertical ZnO nanorods modified by stearic acid. *Ceram. Int.* **2014**, *40*, 7151–7160.

37. Lee, Y.; Zhang, Y.; Ng, S.L.G.; Kartawidjaja, F.C.; Wang, J. Hydrothermal growth of vertical ZnO nanorods. *J. Am. Ceram. Soc.* **2009**, *92*, 1940–1945.

38. Wąsik, P.; Seddon, A.M.; Wu, H.; Briscoe, W.H. Dendritic surface patterns from Bénard-Marangoni instabilities upon evaporation of a reactive ZnO nanofluid droplet: A fractal dimension analysis. *J. Colloid Interface Sci.* **2019**, *536*, 493–498.

39. Wu, H.; Briscoe, W.H. Morphogenesis of polycrystalline dendritic patterns from evaporation of a reactive nanofluid sessile drop. *Phys. Rev. Mater.* **2018**, *2*, 045601.

40. Hu, J.Q.; Li, Q.; Meng, X.M.; Lee, C.S.; Lee, S.T. Thermal reduction route to the fabrication of coaxial Zn/ZnO nanocables and ZnO nanotubes. *Chem. Mater.* **2003**, *15*, 305–308.

41. Riaz, M.; Fulati, A.; Amin, G.; Alvi, N.H.; Nur, O.; Willander, M. Buckling and elastic stability of vertical ZnO nanotubes and nanorods. *J. Appl. Phys.* **2009**, *106*, 1–7.

42. Sun, Y.; Riley, D.J.; Ashfbld, M.N.R. Mechanism of ZnO nanotube growth by hydrothermal methods on ZnO film-coated Si substrates. *J. Phys. Chem. B* **2006**, *110*, 15186–15192.

43. Katwal, G.; Paulose, M.; Rusakova, I.A.; Martinez, J.E.; Varghese, O.K. Rapid Growth of Zinc Oxide Nanotube-Nanowire Hybrid Architectures and Their Use in Breast Cancer-Related Volatile Organics Detection. *Nano Lett.* **2016**, *16*, 3014–3021.

44. Wang, Y.; Cui, Z. Synthesis and photoluminescence of well aligned ZnO nanotube arrays by a simple chemical solution method. *J. Phys. Conf. Ser.* **2009**, *152*, 012021.

45. Wahab, R.; Ansari, S.G.; Kim, Y.S.; Seo, H.K.; Kim, G.S.; Khang, G.; Shin, H.S. Low temperature solution synthesis and characterization of ZnO nano-flowers. *Mater. Res. Bull.* **2007**, *42*, 1640–1648.

46. Gokarna, A.; Parize, R.; Kadiri, H.; Nomenyo, K.; Patriarche, G.; Miska, P.; Lerondel, G. Highly crystalline urchin-like structures made of ultra-thin zinc oxide nanowires. *RSC Adv.* **2014**, *4*, 47234–47239.

47. Hieu, H.N.; Vuong, N.M.; Jung, H.; Jang, D.M.; Kim, D.; Kim, H.; Hong, S.-K. Optimization of a zinc oxide urchin-like structure for high-performance gas sensing. *J. Mater. Chem.* **2012**, *22*, 1127–1134.

48. Taheri, M.; Abdizadeh, H.; Golobostanfard, M.R. Formation of urchin-like ZnO nanostructures by sol-gel electrophoretic deposition for photocatalytic application. *J. Alloys Compd.* **2017**, *725*, 291–301.

49. Shen, G.; Bando, Y.; Lee, C.J. Synthesis and evolution of novel hollow ZnO urchins by a simple thermal evaporation process. *J. Phys. Chem. B* **2005**, *109*, 10578–10583.

50. Elias, J.; Bechelany, M.; Utke, I.; Erni, R.; Hosseini, D.; Michler, J.; Philippe, L. Urchin-inspired zinc oxide as building blocks for nanostructured solar cells. *Nano Energy* **2012**, *1*, 696–705.

51.   Newton, M.C.; Warburton, P.A. ZnO tetrapod nanocrystals. *Mater. Today* **2007**, *10*, 50–54.

52.   Modi, G. Zinc oxide tetrapod: A morphology with multifunctional applications. *Adv. Nat. Sci. Nanosci. Nanotechnol.* **2015**, *6*.

53.   Neykova, N.; Brož, A.; Remeš, Z.; Hruška, K.; Kalbáčová, M.; Kromka, A.; Vaněček, M. ZnO hedgehog-like structures for control cell cultivation. *Appl. Surf. Sci.* **2012**, *258*, 3485–3489.

54.   Bhaskarla, C.; Das, M.; Verma, T.; Kumar, A.; Mahadevan, S.; Nandi, D. Roles of Lon protease and its substrate MarA during sodium salicylate-mediated growth reduction and antibiotic resistance in Escherichia coli. *Microbiol. (United Kingdom)* **2016**, *162*, 764–776.

55.   Sutton, S. Measurement of microbial cells by optical density. *J. Valid. Techn* **2011**, *17*, 46–49.

56.   Schneider, C. a; Rasband, W.S.; Eliceiri, K.W. NIH Image to ImageJ: 25 years of image analysis. *Nat. Methods* **2012**, *9*, 671–675.

57.   Ashiotis, G.; Deschildre, A.; Nawaz, Z.; Wright, J.P.; Karkoulis, D.; Picca, F.E.; Kieffer, J. The fast azimuthal integration Python library: PyFAI. *J. Appl. Crystallogr.* **2015**, *48*, 510–519.

58.   de Gennes, P.-G.; Brochard-Wyart, F.; Quéré, D. *Capillarity and Wetting Phenomena*; 2004; ISBN 978-1-4419-1833-8.

59.   Efroimsky, M.; Gamberg, L.; Gitman, D.; Lazarian, A.; Smirnov, B. *Wetting of Real Surfaces: De Gruyter Studies in Mathematical Physics 19*; ISBN 978-311-02-58-530

60.   Mittal, K. *Contact Angle Wettability and Adhesion*; 2009; ISBN 978-90-04-16932-6.

61.   Wu, X.; Bai, H.; Li, C.; Lu, G.; Shi, G. Controlled one-step fabrication of highly oriented ZnO nanoneedle/nanorods arrays at near room temperature. *Chem. Commun. (Camb).* **2006**, 1655–1657.

62.   Xu, S.; Wang, Z.L. One-dimensional ZnO nanostructures: Solution growth and functional properties. *Nano Res.* **2011**, *4*, 1013–1098.

63.   CLANET, C.; BÉGUIN, C.; RICHARD, D.; QUÉRÉ, D. Maximal deformation of an impacting drop. *J. Fluid Mech.* **2004**, *517*, 199–208.

64.   Han, Z.W.; Wang, Z.; Feng, X.M.; Li, B.; Mu, Z.Z.; Zhang, J.Q.; Niu, S.C.; Ren, L.Q. Antireflective surface inspired from biology: A review. *Biosurface and Biotribology* **2016**, *2*, 137–150.

65.   Diao, Z.; Dirks, J.-H.; Spatz, J. Bio-inspired, nanostructured anti-reflective surfaces for laser applications. *Conf. Lasers Electro-Optics* **2016**, ATh3K.5.

66.   Boden, S.A.; Bagnall, D.M. Tunable reflection minima of nanostructured antireflective surfaces. *Appl. Phys. Lett.* **2008**, *93*, 1–4.

67.   Zada, I.; Zhang, W.; Sun, P.; Imtiaz, M.; Abbas, W.; Zhang, D. Multifunctional , Angle Dependent Antireflection , and Hydrophilic Properties of SiO$_2$ Inspired by Nano-Scale Structures of Cicada Wings. *Appl. Phys. Lett.*, **2017**, 111, 153701.

68.   Chen, Y.C.; Huang, Z.S.; Yang, H. Cicada-Wing-Inspired Self-Cleaning Antireflection Coatings on Polymer Substrates. *ACS Appl. Mater. Interfaces* **2015**, *7*, 25495–25505.

69.   Morikawa, J.; Ryu, M.; Seniutinas, G.; Balčytis, A.; Maximova, K.; Wang, X.; Zamengo, M.; Ivanova, E.P.; Juodkazis, S. Nanostructured antireflective and thermoisolative cicada wings. *Langmuir* **2016**, *32*, 4698–4703.

70.   Tripathy, A.; Sen, P. Dragonfly wing inspired multifunctional antireflective superhydrophobic surfaces. In Proceedings of the 2016 3rd International Conference on Emerging Electronics (ICEE); 2016; pp. 1–3.

71.   Cai, J.; Qi, L. Recent advances in antireflective surfaces based on nanostructure arrays. *Mater. Horiz.* **2015**, *2*, 37–53.

72.   Liu, S.; Killen, E.; Lim, M.; Gunawan, C.; Amal, R. The effect of common bacterial growth media on zinc

oxide thin films: identification of reaction products and implications for the toxicology of ZnO. *RSC Adv.* **2014**, *4*, 4363–4370.

73. Tripathy, A.; Sen, P.; Su, B.; Briscoe, W.H. Natural and bioinspired nanostructured bactericidal surfaces. *Adv. Colloid Interface Sci.* **2017**, 248, 85-104.

74. Ivanova, E.P.; Hasan, J.; Webb, H.K.; Gervinskas, G.; Juodkazis, S.; Truong, V.K.; Wu, A.H.F.; Lamb, R.N.; Baulin, V.A.; Watson, G.S.; et al. Bactericidal activity of black silicon. *Nat. Commun.* **2013**, *4*, 1–7.

75. Li, X.; Cheung, G.S.; Watson, G.S.; Watson, J.A.; Lin, S.; Schwarzkopf, L.; Green, D.W. The nanotipped hairs of gecko skin and biotemplated replicas impair and/or kill pathogenic bacteria with high efficiency. *Nanoscale* **2016**, *8*, 18860–18869.

76. Tripathy, A.; Pahal, S.; Mudakavi, R.J.; Raichur, A.M.; Varma, M.M.; Sen, P. Impact of Bioinspired Nanotopography on the Antibacterial and Antibiofilm Efficacy of Chitosan. *Biomacromolecules* **2018**, , 19, 4, 1340-1346.

77. Zanni, E.; Bruni, E.; Chandraiahgari, C.R.; De Bellis, G.; Santangelo, M.G.; Leone, M.; Bregnocchi, A.; Mancini, P.; Sarto, M.S.; Uccelletti, D. Evaluation of the antibacterial power and biocompatibility of zinc oxide nanorods decorated graphene nanoplatelets: New perspectives for antibiodeteriorative approaches. *J. Nanobiotechnology* **2017**, *15*, 1–12.

78. Okyay, T.O.; Bala, R.K.; Nguyen, H.N.; Atalay, R.; Bayam, Y.; Rodrigues, D.F. Antibacterial properties and mechanisms of toxicity of sonochemically grown ZnO nanorods. *RSC Adv.* **2015**, *5*, 2568–2575.

79. Rago, I.; Chandraiahgari, C.R.; Bracciale, M.P.; De Bellis, G.; Zanni, E.; Cestelli Guidi, M.; Sali, D.; Broggi, A.; Palleschi, C.; Sarto, M.S.; et al. Zinc oxide microrods and nanorods: different antibacterial activity and their mode of action against Gram-positive bacteria. *RSC Adv.* **2014**, *4*, 56031–56040.

80. Li, X.; Chen, T. Enhancement and suppression effects of a nanopatterned surface on bacterial adhesion. *Phys. Rev. E* **2016**, *93*, 1–7.

81. Zhang, X.; Wang, L.; Levänen, E. Superhydrophobic surfaces for the reduction of bacterial adhesion. *RSC Adv.* **2013**, *3*, 12003.

82. Ma, J.; Sun, Y.; Gleichauf, K.; Lou, J.; Li, Q. Nanostructure on taro leaves resists fouling by colloids and bacteria under submerged conditions. *Langmuir* **2011**, *27*, 10035–10040.

83. Truong, V.K.; Webb, H.K.; Fadeeva, E.; Chichkov, B.N.; Wu, A.H.F.; Lamb, R.; Wang, J.Y.; Crawford, R.J.; Ivanova, E.P. Air-directed attachment of coccoid bacteria to the surface of superhydrophobic lotus-like titanium. *Biofouling* **2012**, *28*, 539–550.

84. Stallard, C.P.; McDonnell, K.A.; Onayemi, O.D.; O'Gara, J.P.; Dowling, D.P. Evaluation of protein adsorption on atmospheric plasma deposited coatings exhibiting superhydrophilic to superhydrophobic properties. *Biointerphases* **2012**, *7*, 1–12.